



Evidence for Reduced, Carbon-rich Regions in the Solar Nebula from an Unusual Cometary Dust Particle

Bradley T. De Gregorio¹ , Rhonda M. Stroud¹, Larry R. Nittler² , and A. L. David Kilcoyne³

¹Materials Science and Technology Division, Naval Research Laboratory, Code 6366, 4555 Overlook Avenue SW, Washington, DC 20375, USA; bradley.degregorio@nrl.navy.mil

²Department of Terrestrial Magnetism, Carnegie Institution of Washington, 5241 Broad Branch Road NW, Washington, DC 20015, USA

³Advanced Light Source, Lawrence Berkeley National Laboratory, 1 Cyclotron Road, Mailstop 7R0222, Berkeley, CA 94720, USA

Received 2016 September 6; revised 2017 August 31; accepted 2017 September 10; published 2017 October 20

Abstract

Geochemical indicators in meteorites imply that most formed under relatively oxidizing conditions. However, some planetary materials, such as the enstatite chondrites, aubrite achondrites, and Mercury, were produced in reduced nebular environments. Because of large-scale radial nebular mixing, comets and other Kuiper Belt objects likely contain some primitive material related to these reduced planetary bodies. Here, we describe an unusual assemblage in a dust particle from comet 81P/Wild 2 captured in silica aerogel by the NASA *Stardust* spacecraft. The bulk of this $\sim 20 \mu\text{m}$ particle is comprised of an aggregate of nanoparticulate Cr-rich magnetite, containing opaque sub-domains composed of poorly graphitized carbon (PGC). The PGC forms conformal shells around tiny 5–15 nm core grains of Fe carbide. The C, N, and O isotopic compositions of these components are identical within errors to terrestrial standards, indicating a formation inside the solar system. Magnetite compositions are consistent with oxidation of reduced metal, similar to that seen in enstatite chondrites. Similarly, the core–shell structure of the carbide + PGC inclusions suggests a formation via FTT reactions on the surface of metal or carbide grains in warm, reduced regions of the solar nebula. Together, the nanoscale assemblage in the cometary particle is most consistent with the alteration of primary solids condensed from a C-rich, reduced nebular gas. The nanoparticulate components in the cometary particle provide the first direct evidence from comets of reduced, carbon-rich regions that were present in the solar nebula.

Key words: astrochemistry – comets: individual (81P/Wild 2)

1. Introduction

Comets are relatively pristine reservoirs of early solar system materials. Among the dust particles collected from the Jupiter-family comet 81P/Wild 2 by the NASA *Stardust* mission are early nebular condensates (Brownlee et al. 2006, 2012), chondrule-like materials (Nakamura et al. 2008; Ogliore et al. 2012; Joswiak et al. 2014), presolar grains (McKeegan et al. 2006; Stadermann et al. 2008; Leitner et al. 2010; Floss et al. 2013; Brownlee 2014), and solid carbonaceous matter (Sandford et al. 2006; Cody et al. 2008a; Matrajt et al. 2008; Wirrick et al. 2009; De Gregorio et al. 2011). The predominance of mineral solids in the *Stardust* collection with a presumed inner solar system origin indicates that outward transport of nebular dust was efficient, resulting in a relatively well-mixed nebula (Bockelée-Morvan et al. 2002; Ciesla 2007). Furthermore, detailed analyses of major and minor elements in olivine and pyroxene grains indicate affinities with multiple chondrite classes (Zolensky et al. 2008; Nakashima et al. 2012, 2015; Frank et al. 2014), suggesting that full-scale nebular mixing was still efficient while localized asteroid-forming regions were beginning to form.

Most chondritic meteorites are oxidized relative to the highly reducing conditions of a gas of solar composition (Krot et al. 2000), as indicated by the coexistence of Fe in both metallic and oxidized form. In contrast, enstatite chondrites, which contain abundant Fe-poor pyroxene and Si-rich Fe, Ni-metal, with various sulfide, phosphide, nitride, and carbide phases (Keil 1968; Weisberg & Kimura 2012), are highly reduced. The surface composition of Mercury, as measured in orbit by the *MESSENGER* spacecraft, is also consistent with the accretion of highly reduced precursor materials (Nittler

et al. 2011; Zolotov et al. 2013). Thus, meteoritic and planetary evidence indicates that the solar nebula experienced large variations in redox conditions. This is also supported by measurements of comet Wild 2 samples and chondritic porous interplanetary dust particles (IDPs), thought to originate largely in comets, both of which show a range of oxidation states (Ogliore et al. 2010). One possible cause for the formation of particles in the solar nebula with lower oxidation states is a higher local C/O ratio in the gas (e.g., by addition and evaporation of C-rich dust). For example, Krot et al. (2000) used condensation modeling to constrain the formation region of enstatite chondrites to have a C/O ratio between 0.95 and 1.00, in contrast to the average solar value of ~ 0.5 . It should be noted, though, that Ebel & Alexander (2011) predicted similarly reduced condensates through the addition of anhydrous, IDP-like dust (based on a CI chondrite composition with water of hydration removed). Reduced condensates were generated in this model, despite its lower-than-solar C/O ratio of 0.2, because the decreased total O abundance, leads to O starvation in the gas phase. A similar composition of gas with higher C/O would presumably lead to even more reducing conditions. Independent of the local C/O conditions, if efficient nebular mixing occurred during the accretion of comet Wild 2, then it is possible that reduced and C-rich mineral assemblages reminiscent of those of enstatite chondrites, in addition to oxidized phases from other source regions, might also be present in the *Stardust* sample collection.

Here, we describe the detailed mineralogy of an unusual particle from comet Wild 2 that may have an affinity with the enstatite chondrite-forming region. Recently, a Ni-poor kamacite

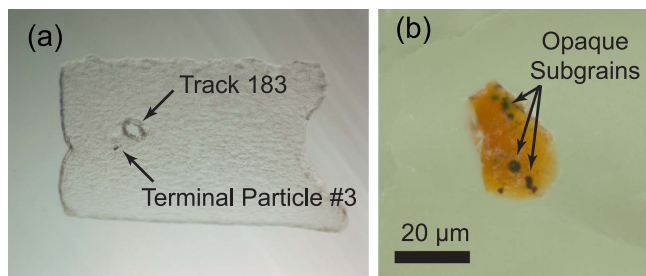


Figure 1. (a) Aerogel wafer cross-section of *Stardust* Track 183, including terminal particle #3. (b) Particle C2103,24,183,1,0 embedded in S after ultramicrotome sectioning (“potted butt”) under dark-field reflected light illumination. Several opaque inclusions are visible in the particle.

grain from Wild 2 was reported to have compositional similarities to enstatite chondrite metal, but shows stronger affinity with metal from ureilites (Humayun et al. 2015). Thus, the particle described herein represents the first evidence from comets of materials condensed in highly reducing environments in the early solar nebula.

2. Methods

2.1. Sample Preparation

Cometary particles in the *Stardust* sample collection exist as μm sized grains at the terminus or along the walls of hypervelocity impact tracks in a low-density silica aerogel (Brownlee et al. 2006). *Stardust* sample C2103,24,183,0,0 is a transverse wafer through capture track 183, containing an oblong $20\ \mu\text{m} \times 30\ \mu\text{m}$ particle at the terminus of the second offshoot from the main capture track (Figure 1(a)). The particle was extracted from the wafer by repetitive puncturing of the aerogel using a fresh glass needle held by a micromanipulator. This procedure was accomplished using an EXpressLO ex situ liftout system within a clean enclosure. Following the *Stardust* sample nomenclature, the extracted particle was given the designation C2103,24,183,1,0. The particle was then embedded in elemental S by melting a 1–2 μm sized pellet of ultrapure S (99.999% pure; STREM Chemicals product 93–1616) on a Bioscience Tools temperature-controlled plate kept at 114°C. During embedding, the aerogel surrounding the particle separated, leaving a bare grain once the S cooled and crystallized (Figure 1(b)). The crystallized S droplet was attached to a standard size “00” epoxy stub using a small amount of cyanoacrylate adhesive.

Multiple ultrathin sections of the embedded particle were prepared with a Leica EM UC7 microtome, outfitted with a Diatome Ultra 45° diamond knife. Sections were placed on one of three different sample mounts. 200-mesh “thinbar” Cu transmission electron microscopy (TEM) grids with a continuous amorphous carbon support film were used for identifying mineral components by TEM. 200-mesh “thinbar” Cu TEM grids with a continuous SiO_x support film were used for characterization of carbonaceous components by scanning-transmission X-ray microscopy (STXM). Thicker sections were made and placed on Si_3N_4 “windows” for isotopic composition measurements by secondary ion mass spectrometry (SIMS). However, since all sections placed on the Si_3N_4 mounts migrated away from the window region of the mount and settled instead on the frame region of the mount, future work can reduce the cost of materials by using bare Si chips. Specific details on the particular samples analyzed for this study are

listed in Table 1. Several months after the first series of ultramicrotome sections were prepared, a second series of sections were attempted. Unfortunately, the S had aged in the intervening time, and the particle was immediately plucked out during the first microtome slice. To avoid this kind of sample loss in the future, the surface of the S could be remelted and recrystallized using a point heat source (such as a soldering iron). It is also possible that long-term storage under dry N_2 gas could protect the potted butt from loss of sulfur through oxidation.

2.2. Transmission Electron Microscopy

Identification and nanoscale characterization of ultramicrotomed slices of the Track 183 particle were carried out with a 200 keV JEOL 2200FS TEM at the Naval Research Laboratory (NRL). Samples were observed in both conventional TEM bright field mode and in scanning (i.e., STEM) mode with a nominal probe size of 0.7 nm, using a high-angle annular dark field (HAADF) STEM detector. In HAADF images, the image intensity is $\sim tZ^{1.7}$, where t is the sample thickness and Z is the average atomic number. For the relatively flat ultramicrotome samples, brightness is directly related to the elemental composition of the material. Crystalline materials were identified by a combination of selected area electron diffraction (SAED) and energy-dispersive X-ray spectrometry (EDS) with a Thermo Noran SYSTEM SIX spectrometer. The elemental compositions of bulk components in the sample were estimated by the quantification of EDS spectra with Noran SYSTEM SIX software (NSS 3.1), using a Cliff–Lorimer routine with library k factors.

High-resolution characterization of individual nanoparticulate components was performed with an aberration-corrected Nion UltraSTEM 200 at NRL, operated at 200 keV. Because this is an ultra-high vacuum instrument, the sample was baked at 140°C for 8 hr under vacuum prior to insertion into the microscope. A nominal probe size of 140 pm was used with a current of 100 pA. The energy spread (measured as the full-width half-maximum of the zero-loss peak in the energy-loss spectrum) of the 200 keV electron beam under these operating conditions was measured to be 0.32 eV in vacuum. The electronic structure and bonding of individual C- and Fe-bearing nanoparticles was observed by electron energy-loss spectroscopy (EELS) with a Gatan Enfinium ER EEL spectrometer. In addition, the elemental compositions of these components were analyzed with high-spatial-resolution EDS mapping using a Bruker windowless silicon-drift detector with a collection angle of 0.7 sr. The EDS spectra were quantified with Bruker Esprit 1.93 software, with a Cliff–Lorimer routine and calculated k factors.

2.3. Scanning-transmission X-Ray Microscopy

Additional chemical mapping was performed with the scanning-transmission X-ray microscope (STXM) at beamline 5.3.2.2 at the Advanced Light Source (Kilcoyne et al. 2003). Utilizing the coherent, monochromated X-ray source, X-ray absorption near-edge structure (XANES) spectra were obtained with a maximum energy resolution of 0.1 eV and a spatial resolution of ~ 30 nm. STXM data were acquired as a sequence of individual X-ray absorption images at different photon energies, which were subsequently aligned to form a spectral image “stack” (Jacobsen et al. 2000). Chemical maps were

Table 1
Samples Characterized in This Study

Sample Number	Thickness	Sample Mount	Additional Information
C2103,24,183,0,0	Aerogel wafer
C2103,24,183,1,0	$20 \times 30 \mu\text{m}$	Embedded in S	Potted butt (lost)
C2103,24,183,1,11	80 nm	200-mesh “thinbar” grid, amorphous C support film	Four sections
C2103,24,183,1,14	80 nm	200-mesh “thinbar” grid, SiO_x support film	Four sections
C2103,24,183,1,18	150 nm	200-mesh “thinbar” grid, amorphous C support film	Four sections
C2103,24,183,1,28	150 nm	Si_3N_4 window	One section
C2103,24,183,1,30	80 nm	200-mesh “thinbar” grid, SiO_x support film	Two sections
C2103,24,183,1,31	80 nm	200-mesh “thinbar” grid, amorphous C support film	Five sections
C2103,24,183,1,33	150 nm	Si_3N_4 window	Three sections

generated by calculating the log-ratio of two images (e.g., a 708 eV image at maximum absorption of the Fe L_3 peak versus a 701 eV pre-peak image to give a map of Fe abundance) on a pixel-by-pixel basis. Similarly, a XANES spectrum was generated for a region of interest by calculating the log-ratio of summed pixel intensities within the region of interest to those from a background, scaled appropriately to the same integration time.

2.4. Secondary Ion Mass Spectrometry

C, N, and O isotopic compositions were measured with a Cameca NanoSIMS 50L ion microprobe at the Carnegie Institution of Washington (CIW) following standard methods for carbonaceous planetary materials (e.g., De Gregorio et al. 2013). Isotopic images were acquired by rastering a focused (~ 100 nm) Cs^+ ion beam across the sample with simultaneous collection of secondary ions and electrons in multicollection mode. C was measured as C_2^- and N as CN^- ions. Microtomed insoluble organic matter from the carbonaceous chondrite Al Rais was used as a N isotopic standard, while cyanoacrylate adhesive adjacent to the *Stardust* sections was used for C and O standards. NanoSIMS data were processed with the L’image software package (L. Nittler, CIW).

3. Results

3.1. Major Components and Composition

In optical images, *Stardust* terminal particle C2103,24,183,1,0 has a red coloration, suggesting a Fe-bearing material, and also contains several opaque inclusions (Figure 1(b)). Low magnification TEM images indicate that these two components are not single crystal or polycrystalline phases, as are observed in most *Stardust* terminal particles (Joswiak et al. 2012). Instead, both the Fe-bearing phase and the opaque phase consist of aggregated nanoparticulate grains (Figure 2). Elongate, 15–40 nm nanoparticulate laths (with widths of 5–15 nm) comprise the Fe-bearing material (Figure 2(c)), while the opaque inclusions are aggregates of 10–20 nm carbonaceous spherical grains (Figure 2(d)). SAED of $0.5 \mu\text{m}^2$ regions of both materials show diffraction rings typical of randomly oriented nanoparticulate material. As indicated in Table 2, the two diffraction rings in SAED ring patterns from the Fe-bearing material are consistent with the two most intense lattice spacings for a spinel crystal structure, while those from the opaque inclusions are consistent with graphite with an expanded c -axis lattice spacing, commonly observed in poorly graphitized carbon (PGC).

The elemental compositions of these two nanoparticle phases further confirm their identification as Cr-rich magnetite

(Fe-bearing spinel structure) and PGC, respectively. Elemental maps of Fe and C generated from STXM images indicate that the bulk of the terminal particle is Fe-rich, while the opaque inclusions are carbonaceous (Figure 3). C-XANES of the carbonaceous inclusions reveal spectra indicative of PGC, with some additional contribution from carbonyl (C=O) functional groups (Figure 4). The presence of O in the PGC is consistent with the expanded c -axis lattice spacing (Table 2). Assuming a spinel stoichiometry based on the inferred crystal structure of the Fe-bearing phase, quantification of EDS spot spectra (Table 3) results in the average chemical formula $\text{Fe}_{2.60}\text{Cr}_{0.30}\text{Ni}_{0.09}\text{O}_4$. Very small Si and S peaks are also present in EDS spectra of the magnetite. While the S contribution is due to surface contamination from the S embedding medium, there is no obvious source of Si contamination other than possible mixing with silica aerogel.

3.2. Nanoscale Structure of Core-shell Grains in Opaque Carbonaceous Inclusions

Closer inspection of the PGC nanoparticles that comprise the opaque carbonaceous inclusions reveals that these nanoparticles also include discrete electron-dense crystalline grains that are Fe-rich (Figure 5). PGC forms concentric shells on the surfaces of these grains, up to 6 nm (approximately 16–18 layers) on the largest core grains. Due to this core-shell structure, and the small size of the grains, SAED patterns of individual core-shell nanoparticles were dominated by PGC diffraction spots. However, crystal lattice fringes visible in HRTEM images of Fe-rich core grains showed variable lattice spacings between 2.09–2.19 Å and 2.27–2.36 Å. Since these crystalline core grains only contain Fe, and possibly C (Figure 5(c)), their mineralogy is constrained to be Ni-free Fe-metal or carbide. Both body centered cubic and cubic close packed Fe-metal crystal structures have major lattice spacings of 2.03 and 2.07 Å, respectively (Wyckoff 1963), neither of which are consistent with the observed lattice fringes in the cometary core-shell grains. However, the most common Fe carbide phase in planetary materials, cohenite (orthorhombic Fe_3C —also known as cementite), does contain major lattice spacings of 2.107, 2.218, 2.262, and 2.381 Å (Herbstein & Smuts 1964), all of which could be consistent with the observed grains. Since single-phase SAED patterns without the inclusion of PGC diffraction spots could not be acquired, the core grains could also be composed of other Fe carbide phases, such as the low temperature ϵ (hexagonal Fe_3C) or Hägg (Fe_5C_2) carbides, which have similar lattice spacings. The core grain shown in Figure 6(d) contains intergrowths of two carbide phases, creating a Moiré pattern across the grain.

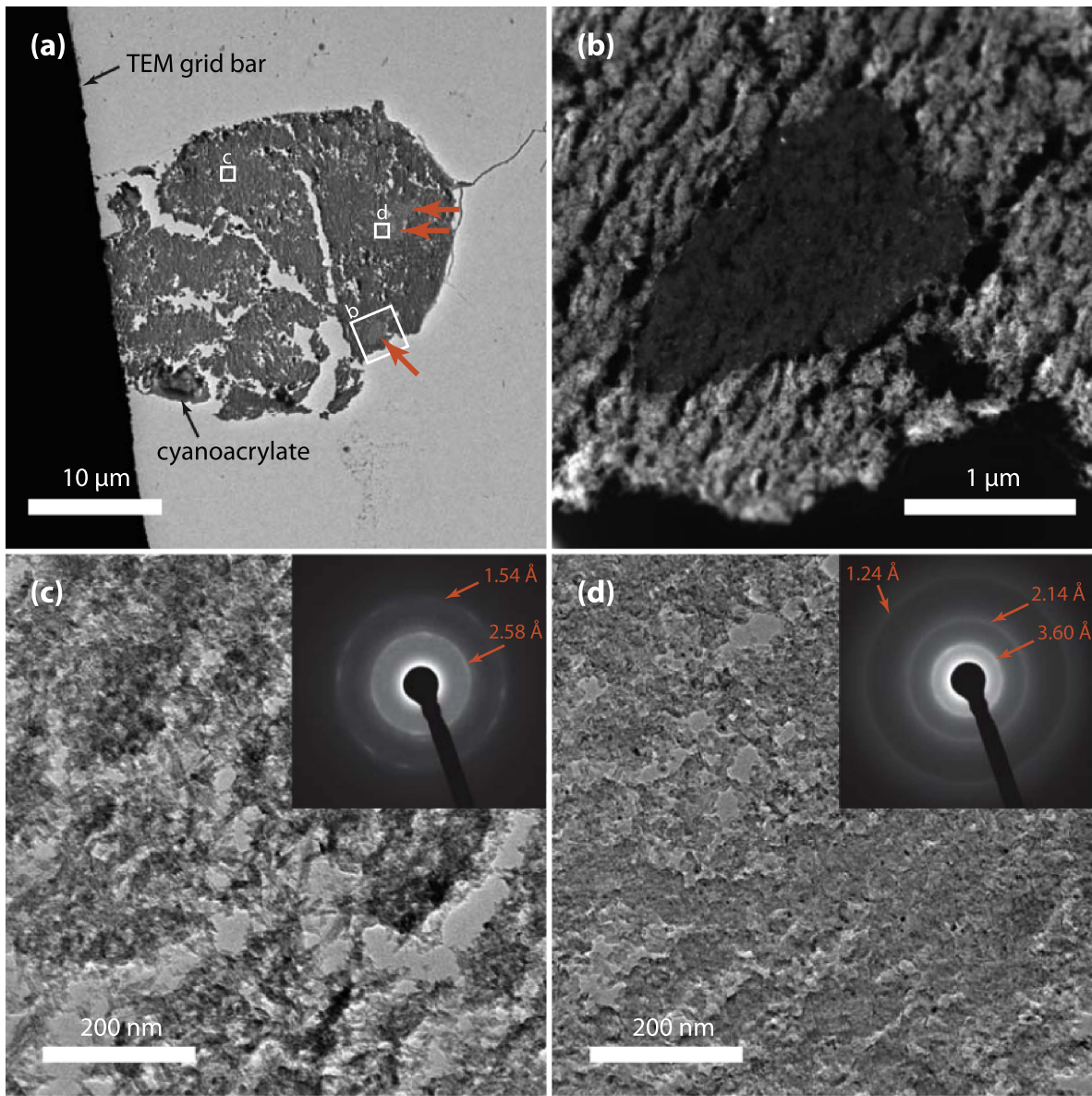


Figure 2. (a) Bright-field TEM image of C2103,24,183,1,31. Three carbonaceous inclusions within this ultramicrotome section are marked by arrows. (b) HAADF STEM image of one of the carbonaceous inclusions, showing lower scattering intensity relative to the surrounding Fe-bearing phase. Bright-field TEM images of the (c) Fe-bearing phase and (d) opaque inclusions show that they both consist of nanoparticulate material. SAED patterns for each phase (insets) reveal diffraction rings consistent with spinel and graphitic phases, respectively.

Table 2

Lattice Spacings (Å) Measured from SAED Ring Patterns

Measured Spacing	Ideal Spacing ^a
<i>Fe-bearing phase</i>	
2.58	2.54 (311)
1.54	1.48 (440)
<i>Opaque inclusion</i>	
3.60	3.35 (002)
2.14	2.13 (100)
1.24	1.23 (110)

Note.

^a Associated crystallographic axis is listed in parenthesis.

Although the exact Fe carbide phases could not be robustly identified, it is clear that none of the core Fe-rich grains are composed of Fe-metal.

3.3. Isotopic Compositions

Three microtomed sections (one section in C2103,24,183,1,28 and two sections in C2103,24,183,1,33) were analyzed by NanoSIMS for C, N, and O isotopic compositions. No isotopic anomalies were observed in N, but the NanoSIMS images indicated that all of the measured N was associated with the Si₃N₄ substrate or residual cyanoacrylate adhesive around the edges of the particle. Bulk O-isotopic ratios of the aggregated magnetite are within errors (100‰ for ¹⁷O/¹⁶O; 15‰ for ¹⁸O/¹⁶O, 1σ errors) of the cyanoacrylate used as an internal standard. Although count rates were sufficient to identify large O isotope anomalies at the 200 nm scale, indicative of a presolar, stellar origin, no such isotopic anomalies were observed in either the magnetite or PGC inclusions. In addition, ¹³C/¹²C ratios in the PGC inclusions were found to be identical within 30‰ (1σ errors) to that of the cyanoacrylate adhesive. For the largest PGC inclusions, such as the one shown in Figure 6, the C isotope

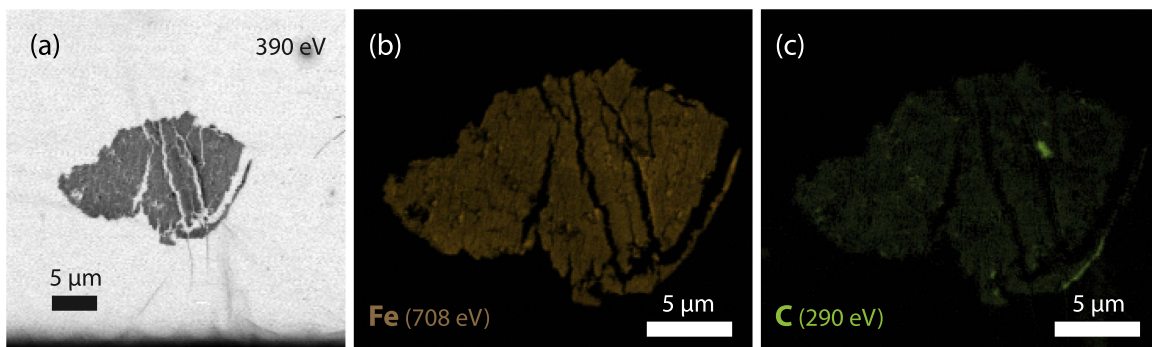


Figure 3. (a) STXM image of C2103,24,183,1,30 acquired at 390 eV. (b) Fe absorption “map” generated by the log-ratio of peak Fe absorption at 708 eV to pre-edge background absorption. (c) C absorption map using a peak energy of 290 eV. This microtome section contains a single large carbonaceous inclusion, with two smaller inclusions near the bottom edge of the particle. C absorption along the edges of the particle is due to cyanoacrylate infiltration.

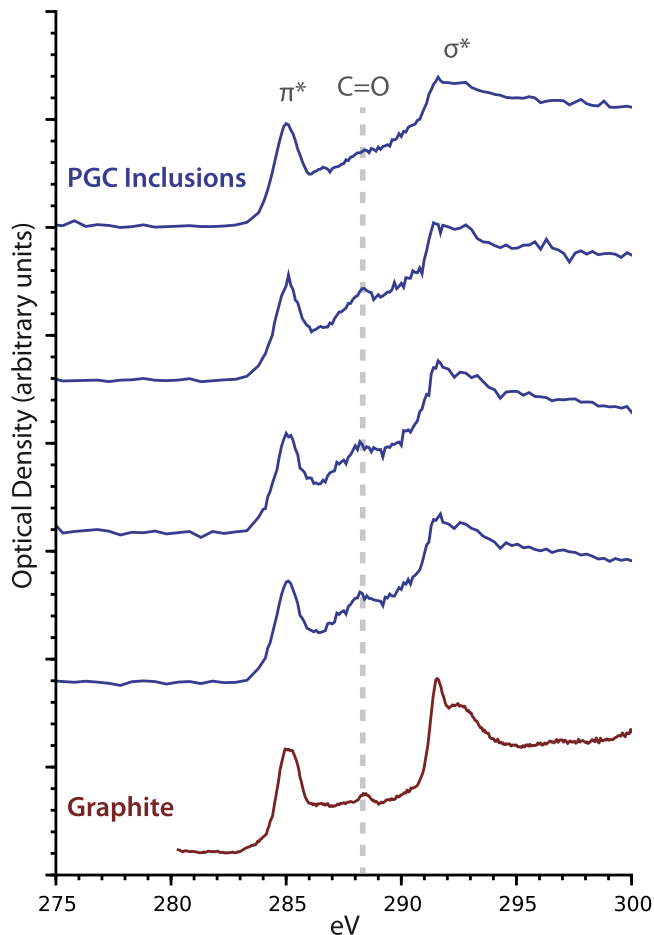


Figure 4. C-XANES spectra of carbonaceous inclusions in C2103,24,183,1,14 and C2103,24,183,1,30. The spectra show X-ray absorption features indicative of PGC (as observed in a disordered graphite standard), with additional contribution at 288.5 eV due to carbonyl (C=O) functional groups (dashed line). Spectra are offset along the vertical axis.

compositions match our internal terrestrial standard to within 5‰ (1σ error). These terrestrial-like O- and C-isotopic ratios of the *Stardust* particle support an origin in the early solar system.

4. Discussion

The mineral assemblage present in the Track 183 terminal particle (Cr-rich magnetite + PGC + Fe carbide) has not been

previously reported in cometary grains from the *Stardust* collection, although some individual components have. Here we will review the known origins for these components in both the *Stardust* collection and in other planetary materials, and describe the most plausible scenario for their collective formation.

4.1. Origin of PGC + Carbide Core-shell Nanoparticles

4.1.1. Fe Carbide in Planetary Materials

The least abundant, yet presumably the first formed, component of the track 183 terminal particle, Fe carbide, has not been previously reported from the *Stardust* collection. Fe carbides are also relatively rare in chondritic meteorites, although they are more prevalent in iron meteorites (Brett 1966). Fe carbides are occasionally observed in low metamorphic grade CO and unequilibrated ordinary chondrite meteorites (Scott & Jones 1990; Shibata 1996), and mineral textures and crystallographic relationships in these samples indicate that the Fe carbide formed from accreted metal grains during initial parent-body heating up to 500°C (Krot et al. 1997; Keller 1998). In addition, there is evidence that Fe carbide may form from contact metamorphism of primary metal grains with shock-induced melts (Hauver & Ruzicka 2011). Fe carbides, specifically cohenite, are also observed in enstatite chondrites (Ramdohr 1973) as part of the overall assemblage of reduced minerals in those meteorites (Keil 1968). In this case, the cohenite is interpreted as a preaccretionary nebular condensate, along with the other highly reduced minerals (e.g., various sulfides, nitrides, and Si-bearing metal), consistent with a nebular gas ratio of $0.95 < C/O < 1.00$ (Krot et al. 2000).

Nebular condensation models predict that cohenite can condense before ferromagnesian silicates and oxides when $C/O > 1.0$, and will dominate over condensation of metal grains when $C/O > 1.01$ (Figure 7; Krot et al. 2000; Ebel 2006). These same models predict that metal grains condense as the gas temperature falls below 1180°C regardless of the C/O ratio, except at $C/O > 1.01$, where the condensation temperature falls by 40°C (Ebel 2006).

4.1.2. PGC in Planetary Materials

Reports of PGC or graphite in the *Stardust* sample collection are rare. Graphitic lattice fringes were observed in TEM images of carbonaceous matter preserved in the “Coki” terminal particle of track 141 (Matrajt et al. 2013). In addition, Raman spectroscopy of the terminal particle of track

Table 3
Elemental Composition (wt. %) of Nanoparticulate Magnetite from EDS Spectra

Sample	MgO	Al ₂ O ₃	SiO ₂	CaO	TiO ₂	Cr ₂ O ₃	MnO	FeO	NiO	ZnO	Fe (mol)	Cr (mol)	Ni (mol)
Spot 1	0.13	0.31	5.79	0.65	<i>n.d.</i>	5.48	0.43	83.61	3.26	0.35	0.910	0.056	0.034
Spot 2	<i>n.d.</i>	0.48	4.15	0.55	<i>n.d.</i>	14.40	0.20	76.53	3.34	0.34	0.820	0.146	0.034
Spot 3	0.07	0.35	4.00	0.42	0.03	7.73	0.58	84.31	2.35	0.16	0.898	0.078	0.024
Spot 4	0.06	0.46	7.48	0.56	<i>n.d.</i>	11.63	0.45	76.31	2.71	0.33	0.848	0.122	0.029
Spot 5	0.03	0.31	2.84	0.72	<i>n.d.</i>	8.59	0.43	83.96	2.92	0.21	0.885	0.086	0.030
Spot 6	0.06	0.51	4.77	0.67	0.03	12.84	0.27	77.56	2.99	0.30	0.838	0.131	0.031
Spot 7	0.06	0.56	3.74	0.45	<i>n.d.</i>	8.26	0.27	83.91	2.54	0.21	0.891	0.083	0.026
Average	0.06	0.426	4.68	0.57	0.01	9.85	0.38	80.88	2.87	0.27	0.870	0.100	0.030

81 showed a sharp G band at 1576 cm^{-1} , consistent with graphitic carbon (Fries et al. 2009). Other than these two examples, all other occurrences of solid carbonaceous matter from Wild 2 appear to be nongraphitized aliphatic or aromatic macromolecular material (Matrajt et al. 2008; De Gregorio et al. 2011; Matrajt et al. 2013). These terminal grains were collected in the *Stardust* aerogel collector at 6.1 km s^{-1} , and thus could potentially have experienced significant flash heating as they were slowed during capture (Leroux et al. 2008; Rietmeijer et al. 2008), which could have initiated graphitization of cometary organic matter. However, the presence of low temperature sulfides in the *Stardust* collection (Berger et al. 2011), light-gas gun experiments (Burchell et al. 2006), and the predominantly ungraphitized carbonaceous matter (Matrajt et al. 2008, 2013; De Gregorio et al. 2011) indicate that many of the captured Wild 2 terminal particles did not experience temperatures above 200°C . Since the track 183 terminal particle contains a nanoparticle microstructure with no melted cometary material or aerogel, we infer that it was not heated upon capture to a significant degree, and therefore the PGC inclusions are an additional find of indigenous cometary graphitic carbon from Wild 2.

PGC is the most prevalent carbonaceous phase in heated chondrites of petrologic type 3.2–3.7, where thermal metamorphism on asteroid parent bodies has led to graphitization of accreted organic matter (Quirico et al. 2003; Le Guillou et al. 2012). This process is also the source of the PGC comprising the “graphite-magnetite” assemblages discussed in Section 4.2.2, which originally accreted as nongraphitic organic matter (Brearley 1990). At petrologic type 3.7 and above, large domains of crystalline graphite occur (Busemann et al. 2007; Cody et al. 2008b). Graphite can also form as exsolution lamellae in C-bearing Fe, Ni-metal grains, mainly studied in lodranites and acapulcoites (El Goresy et al. 1995; McCoy et al. 2006; Charon et al. 2014a), but also observed in ordinary chondrites (Mostafaoui et al. 2000). Exsolved graphite is the dominant carbonaceous phase in enstatite chondrites (Rubin 1997; Remusat et al. 2012). Heating of carbonaceous matter in the presence of metal grains above 900°C can also generate PGC (Charon et al. 2014b). These formation pathways require high-temperature conditions that did not occur on Wild 2, but such environments did exist in warm inner regions of the protoplanetary disk where condensation was occurring. Thus, it is more likely that the PGC inclusions in the track 183 terminal particle were created by reaction of nebular carbonaceous matter with metal or Fe carbide dust grains, rather than by heating on Wild 2 itself.

4.1.3. Catalysis of PGC on Fe Carbide and/or Metal Grains

When considered together, the closest planetary materials analogs to the track 183 PGC + cohenite core-shell grains are rare Fe carbides (both ϵ carbide and cohenite) coated by 2–10 nm of layered PGC, found in anhydrous chondritic IDPs (Bradley et al. 1984; Keller et al. 2004). In addition, clumps of “core-less” PGC particles with diameters up to 50 nm are also observed (Rietmeijer & Mackinnon 1985; Rietmeijer 1992). The size ranges for the PGC coatings and particles are consistent with those in the track 183 terminal particle, although the Fe carbide grains in the IDP samples are an order of magnitude larger than those in track 183. The PGC coatings on IDP carbides have been attributed to sustained heating during atmospheric entry of the dust aggregates prior to collection (Keller et al. 2004), but early researchers also proposed nebular Fischer-Tropsch-type (FTT) reactions catalyzed on the surface of Fe carbide or metal grains (Hayatsu & Anders 1981; Bradley et al. 1984). Peak temperature and heating timescales for IDPs depends on several factors, including particle size, velocity, entry angle, and the occurrence of aerobraking “bounces” that effectively lower the entry velocity (Love & Brownlee 1991). For typical chondritic IDPs, the particles experience heating to temperatures above 300°C for about 10 s, with a peak temperature around 1500°C (Love & Brownlee 1991), which may be adequate to graphitize existing carbonaceous matter in the particle. On the other hand, FTT experiments mimicking warm nebular conditions on both Fe-metal and graphite catalysts overwhelmingly produce PGC instead of nongraphitized carbonaceous matter (Nuth et al. 2008, 2010). Furthermore, FTT synthesis is known to cause carburization of metal grains to form carbides (Raupp & Delgass 1979; Niemantsverdriet et al. 1980), so FTT synthesis catalyzed by preaccretionary metal grains could also result in carbide core grains. These studies also reported the complete transformation of metal into carbide in nanoparticles with diameters of up to 30 nm. Considering that the carbide cores in track 183 are all nanoparticulate ($<20\text{ nm}$), the complete transformation from nanoparticulate metal condensates into cohenite core grains, leaving no residual metal, during nebular FTT reactions is plausible.

Given that temperatures on comet Wild 2 could not allow the generation of PGC and/or carbide minerals, these components of the track 183 terminal particle must have either formed prior to accretion or during sample collection during the *Stardust* encounter with the comet. The lack of melt features in the enclosing nanoparticulate magnetite or melted silica aerogel in the track 183 terminal particle indicates that the flash heating during capture could not be responsible for PGC + cohenite

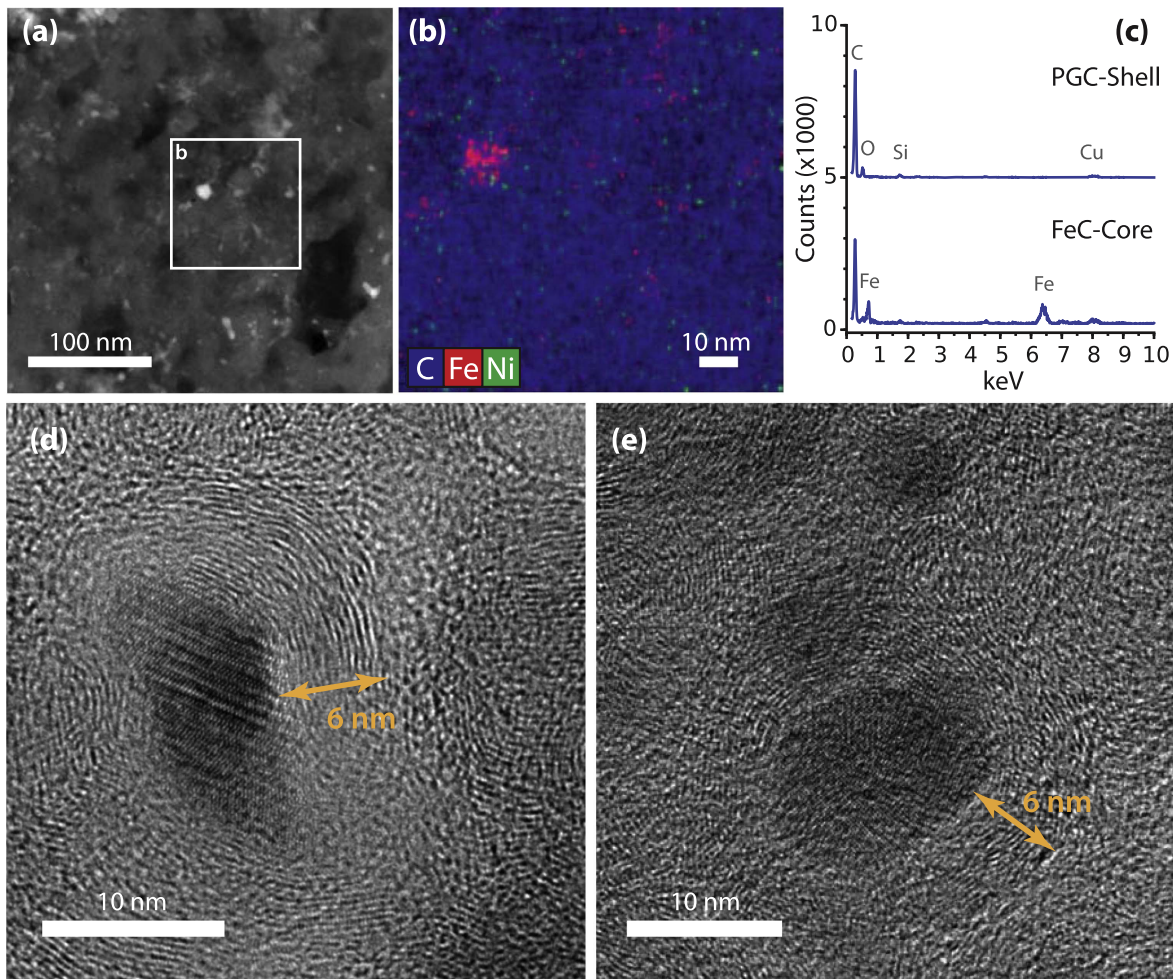


Figure 5. (a) HAADF image of PGC peppered with bright sub-grains with a high average atomic mass. (b) EDS elemental map of the region surrounding a 10 nm Fe-rich sub-grain. The Ni counts are included to show that no Ni is present in the FeC core grains above background noise. (c) EDS spectra from this Fe-rich grain and surrounding PGC. Spectra are offset along the vertical axis. The minor Cu peaks are due to fluorescence from the Cu TEM support grid. (d)–(e) HRTEM images of core–shell grains. PGC forms 6 nm shells around the largest Fe-rich cores.

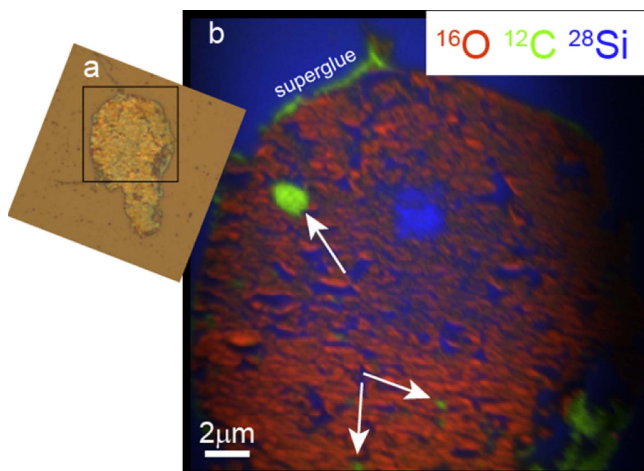


Figure 6. (a) Reflected light image of an ultramicrotome section of C2103,24,183,1,28. (b) False color NanoSIMS ion image of the sample (box in part a) showing the distribution of $^{16}\text{O}^-$, $^{12}\text{C}_2^-$, and $^{28}\text{Si}^-$ secondary ion signals. White arrows indicate locations of carbonaceous inclusions within the main magnetite phase. The large PGC inclusion near the upper left is the same inclusion as shown in Figure 2(b), but in an adjacent ultramicrotome section. Some cyanoacrylate adhesive is present around the edges of the particle in the upper left and lower right portions of the image. The ^{28}Si signal is primarily derived from the Si_3N_4 substrate.

formation from original organic matter and metal nanoparticles. Therefore, these core–shell grains must have formed prior to accretion on Wild 2.

We propose that the simplest and most likely formation mechanism for the unique core–shell nanoscale PGC and cohenite aggregates in the track 183 terminal particle is condensation from a warm, C-rich nebular gas, followed by transport outward to the formation site of Wild 2. The core grains would have condensed either as cohenite or as Ni-poor metal grains, both of which most likely originated in a reduced nebular environment (see Sections 4.1.1 and 4.2.4, respectively), and later converted to carbide during FTT synthesis. Such metal and carbide grains could facilitate decomposition of CO and CH_4 gas by FTT reactions to form PGC. Alternatively, if $\text{C}/\text{O} > 0.95$, graphite, including PGC, could directly condense on the surface of these grains (Figure 7). Once graphite and/or PGC exist on the grains, they become self-catalyzing for FTT synthesis, as long as the nanoparticles remain in a warm region of the nebula (Nuth et al. 2008). This core–shell structure is not predicted to form in a nebular gas where $\text{C}/\text{O} > 1.04$, because above that gas composition PGC/graphite is predicted to condense before cohenite (Figure 7), creating a mixture of PGC and carbide nanoparticles rather than discrete core–shell grains. It is possible, then, that PGC +

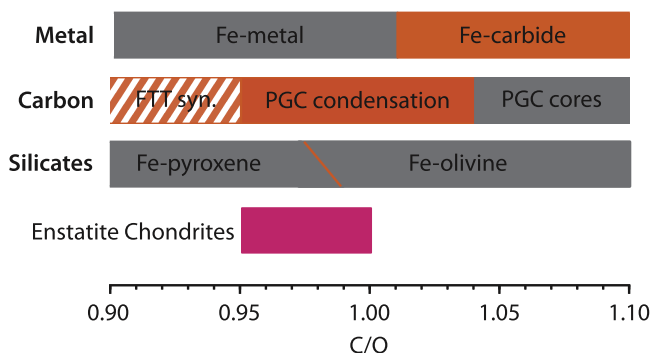


Figure 7. Allowed ranges in carbon/oxygen ratio for condensation from a reduced, C-rich nebular gas between 900 and 1200°C for various Fe- and C-bearing phases, compared to the range estimated for enstatite chondrites (Krot et al. 2000). Predicted condensation ranges are taken from condensation model results described in Ebel (2006).

cohenite core-shell nanoparticles, as observed in track 183, could form from any cooling nebular gas as long as $C/O < 1.04$. At the most reducing conditions in that range ($1.00 < C/O < 1.04$) these core-shell nanoparticles could form directly from the predicted condensation sequence, while at more oxidizing conditions ($C/O < 1.00$), it is more likely that FTT processes played a role in their formation.

4.2. Origin of Nanoscale Magnetite

4.2.1. Magnetite and Chromite in the Stardust Collection

Magnetite and hematite associated with Fe-metal were observed in *Stardust* tracks 41 and 121, and were interpreted as alteration products, either through the aqueous alteration of metal on comet Wild 2 or oxidation of metal during capture heating in the silica aerogel collector (Bridges et al. 2010). Magnetite was also observed with pyrrhotite in the terminal particle of track 134 (Changela et al. 2012), in terminal particles from tracks 178 and 187 (Hicks et al. 2017). Isolated, μm sized grains of magnetite have been reported in the walls of Track 80, also interpreted to result from aqueous alteration on the comet (Stodolna et al. 2012). However, none of the previous magnetite compositions were reported to contain significant Cr content. Several chromite grains have been reported in the *Stardust* collection, from tracks 10, 26, 35, 41, 56, 69, 74, 77, 112, 141, and within a crater residue from the Al foil sample C2043N,1 (Mikouchi et al. 2007; Nakamura et al. 2008; Jacob et al. 2009; Bridges et al. 2010; Stroud et al. 2010; Nakamura-Messenger et al. 2011; Joswiak et al. 2012; Ogliore et al. 2012; Stodolna et al. 2014). However, these chromite grains have Cr:Fe molar ratios around 2, whereas the nanocrystalline magnetite from track 183 only contains a Cr enrichment of 10% (Figure 8).

4.2.2. Aqueous Alteration on Parent Bodies

Magnetite in chondritic meteorites is almost always a product of aqueous alteration of Fe, Ni-metal, and sulfides. These secondary grains have nearly ideal mineral compositions (>95 wt.% Fe + O) in a variety of morphologies, such as framboids and plaquettes (Hua & Buseck 1998). In petrologic type 3 ordinary chondrites, Fe carbides are even found in association with the magnetite in aqueously altered metal grains (Krot et al. 1997), although those Fe carbides readily

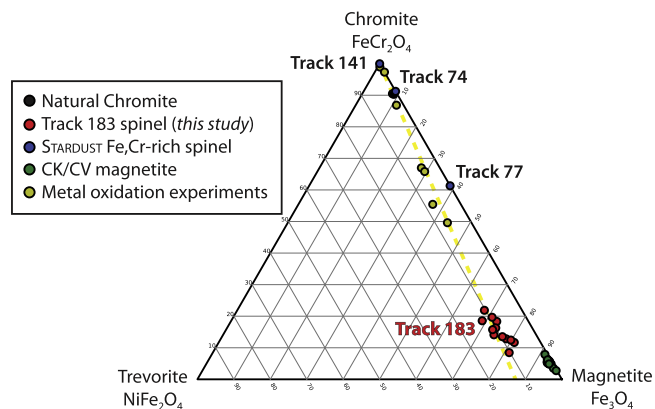


Figure 8. Comparison of compositions of Cr-rich magnetite nanoparticles from *Stardust* track 183, compared with previous Fe- and Cr-rich spinel grains from Wild 2 and Cr-rich magnetite in CK and CV chondrites. Data from chromite and Cr-rich magnetite formed by high-temperature oxidation experiments of Fe, Ni-metal alloys form a compositional trend with the track 183 Cr-rich magnetite (dashed line). References: Joswiak et al. 2012; Ogliore et al. 2012; Greenwood et al. 2010; Righter & Neff 2007; Laurretta & Schmidt 2009.

incorporate Ni and Co from the metal, while the Fe carbides in the track 183 particle contain no Ni (Figure 5(b)). Magnetite with the highest Cr content is seen in CK and CV chondrites (Righter & Neff 2007; Greenwood et al. 2010). However, both the composition (Figure 8) and morphology of the nanoparticulate magnetite in the track 183 terminal particle are distinct from secondary chondritic magnetite. Clasts of μm and sub- μm sized “graphite-magnetite” assemblages were reported from several ordinary chondrite regolith breccias (Scott et al. 1981a, 1981b). However, subsequent TEM studies of these materials revealed that they are composed of PGC encompassing Fe, Ni-metal grains, with no well-ordered graphite, magnetite, or carbide minerals (Brearley 1990). In these assemblages, the initial components (i.e., Fe, Ni-metal, and carbonaceous matter) were hypothesized to have formed in the solar nebula, possibly via FTT synthesis on nebular metal grains, while the transformation of carbonaceous matter into PGC occurred on the parent body. However, since no magnetite was observed in the “graphite-magnetite” assemblages, this proposed mechanism does not inform our understanding of the formation of nanoscale Cr-rich magnetite found in *Stardust* track 183.

4.2.3. Shock Processing on Parent Bodies

Nanoparticulate magnetite has also been hypothesized to form in chondrite meteorites during shock events. While chondritic metal only produces melt veins and/or shock textures in Fe, Ni-metal grains when shocked, shock decomposition of Fe-rich carbonate can produce magnetite. This idea was put forward as an alternative abiotic origin for magnetite nanoparticles in ALHA 84001 that were initially interpreted as the product of ancient magnetotactic Martian microorganisms (Thomas-Keprta et al. 2000; Bell 2007). Both ballistic and pulsed laser shock experiments of natural siderite produced nanoparticulate magnetite (Isambert et al. 2006; Bell 2007). Although some elongated magnetite nanoparticles are produced, similar to those observed in the track 183 terminal particle, the shock-produced magnetite is mostly equant grains. In addition, much of the initial siderite is retained after the shock experiments, while no carbonates were observed in the

track 183 terminal particle. Electron microprobe analysis and EDS of the shock-produced magnetite found minor elements from the initial siderite were retained in the magnetite, including Mg, Mn, and Ca (Isambert et al. 2006; Bell 2007). While Cr is sometimes present in siderite, and therefore could be retained in a shock-produced, Cr-rich magnetite, such a sample would also likely contain traces of Mg, Mn, and Ca, which are not observed in the track 183 magnetite.

4.2.4. Oxidation of Nebular Metal

Magnetite could have formed within the solar nebula by gaseous oxidation of Fe, Ni-metal (Hong & Fegley 1998). Experimental studies of chondritic (Ni-, Cr-, Co-, and P-bearing) metal analog material under high temperature ($>700^{\circ}\text{C}$) early nebular conditions produced both chromite and Cr-rich magnetite on metal surfaces (Lauretta & Schmidt 2009). Although the oxidation products in that study contained much higher Cr content ($>30\%$ Cr) than the track 183 magnetite, they form a compositional tie line (Figure 8), suggesting a similar formation mechanism. However, all minor elements in the starting metal also become incorporated into the magnetite, creating a relic geochemical signature of the original metal. Similar magnetite compositions were also produced by metal oxidation at lower temperatures down to 350°C (Harries 2016). Oxidation of primary condensates (chiefly Fe-rich perovskite) to form magnetite has been observed in a calcium–aluminum-rich inclusion from the CK chondrite Maralinga (Kurat et al. 2002). Nebular oxidation of metal in the presence of ^{16}O -poor water is also invoked to explain the formation of intergrown magnetite/pentlandite cosmic symplectites in ungrouped carbonaceous chondrite Acfer 094 (Sakamoto et al. 2007; Seto et al. 2008).

While nebular oxidation of metal provides a satisfying origin for the nanoparticulate magnetite in track 183, two observations are inconsistent with such a mechanism. First, the track 183 magnetite consists of elongated, prismatic nanoparticles, with no evidence of euhedral octahedral or plaquette crystal forms that are observed in metal oxidation experiments (Harries 2016). Second, the observed compositions of track 183 magnetite do not contain the expected enrichments in Ni and Co that would be created during oxidation of typical chondritic metal. In addition, no evidence of remnant metal or other metal oxidation products, such as chromite, eskolaite, or schreibersite, was found. If we assume the track 183 magnetite formed from metal oxidation, it would imply that (a) the original metal was almost pure Ni-poor kamacite, and (b) a physical separation process efficiently segregated the magnetite not only from the surface of the metal, but also from chromite and any other oxidation products.

Most meteoritic metal contains greater than 3.5 wt.% Ni, except for that found in primitive, metal-rich enstatite (EH3) chondrites (El Goresy et al. 1988; Weisberg & Kimura 2012) and ureilites (Horstmann et al. 2014). Interestingly, both EH3 and ureilite metal contain excess Si (up to 3 wt.% in EH and up to 4.5 wt.% in ureilite), and the track 183 magnetite also contains on average about 5 wt.% SiO_2 (Table 3), although surface contamination from silica aerogel cannot be ruled out. The Si-rich and Ni-poor metal in both EH3 chondrites and ureilites formed in highly reducing environments—EH3 metal through condensation from a reduced nebular gas (Weisberg & Kimura 2012) and ureilite metal through local partial melting with silicates and sulfides (Horstmann et al. 2014). Since the

timeframe in which the metal oxidation could have occurred is constrained by the requirement for transport outward to the Kuiper Belt for accretion onto comet Wild 2, a ureilite metal source can probably be ruled out. However, the possibility of magnetite formation from EH3 chondrite metal, which would have existed prior to the formation of the EH parent body, means that even though the track 183 magnetite would have formed in a more typical (i.e., oxidized) nebular environment, the underlying metal grain (or grains) are indicative of a highly reduced local nebular environment. This also implies that any metal nanoparticles that may have carburized into cohenite during FTT synthesis of PGC to form the core–shell inclusions also likely condensed initially from a highly reduced nebular gas, since otherwise it would require transport of a significant number of metal nanoparticles from a nearby nebular region rather than utilizing the metal grains that would have already been present.

Sub- μm sized metal grains with low Ni compositions are occasionally observed in “dusty” olivine relic grains in chondrules (Rambaldi & Wasson 1982; Jones & Danielson 1997). These nanoscale metal grains can form by sub-solidus heating of fayalitic olivine (and possibly other ferromagnesian chondrule silicates) in a highly reducing gas (Leroux et al. 2003). The composition of these grains is distinct from that of typical chondrule metal, which contains chondritic levels of Ni and other nonvolatile elements (Connolly et al. 2001). While solid state reduction of chondrule olivine could generate an appropriate source of size-selected nanoparticles of nearly pure Fe-metal, it would still require physical destruction of the host olivine in order to free the metal nanoparticles for subsequent oxidation into magnetite, in contrast to an EH chondrite source, for which condensed metal grains would already be free-floating in the nebula. The additional disaggregation step after chondrule silicate reduction makes this process unlikely to be the source of nanoparticulate metal grains that eventually resided as magnetite nanoparticles on comet Wild 2.

4.2.5. Condensation from a Nebular Gas

Although no clear examples have been observed in meteorites, here we consider the possibility of direct condensation of magnetite from a nebular gas of solar composition. This is motivated by the nanoparticulate aggregate nature of the track 183 particle, which suggests a condensation mechanism. While Cr-rich spinels, including magnetite, are predicted to condense at lower temperatures ($<1230^{\circ}\text{C}$) than most phases (Ebel & Grossman 2000), magnetite itself is only predicted to be stable below 400°C in a gas of solar composition (Hong & Fegley 1998), and would only be stable at even lower temperatures in more reducing conditions. Although Fe is most likely to condense as metal grains, or as Fe-carbide when the C/O > 1.01 (Ebel 2006), in a nebula where ice-free, C-rich dust is prevalent, the proportion of Fe condensing directly as metal does not exceed 55% (Ebel & Alexander 2011). However, Fe-bearing olivine, Fe-carbide, and even chromite are still predicted to condense at temperatures well above that required for magnetite (Figure 7). Therefore, we conclude that direct condensation cannot be responsible for the formation of the aggregated magnetite grains in track 183, despite its nanoparticulate texture.

4.3. Assembly of the Track 183 Terminal Particle and Implications for Reduced Environments in the Solar Nebula

It is clear from the presence of PGC + cohenite inclusions within the larger magnetite nanoparticle aggregate that the formation of PGC and cohenite must have preceded magnetite formation. Considering the possible origins of the various components found in the track 183 terminal particle, we seek possible formation pathways that explain this temporal relationship. In addition, although dust grains can travel significant distances within the solar nebula, interacting with many distinct cosmochemical environments (Ciesla & Sandford 2012), the consistent compositional and organic chemical functionality of the multiple PGC + cohenite inclusions within the nanoparticulate magnetite suggests a more likely formation within a single nebular region.

Oxidation of condensed metal grains, producing Cr-rich magnetite, with concurrent catalysis of FTT reactions to generate PGC + cohenite core-shell particles is most consistent with the overall observed mineral relationships and compositions. As discussed above, the formation of magnetite on metal under oxidizing conditions is well known (Hong & Fegley 1998; Lauretta & Schmidt 2009), if this occurred in an ice-rich and/or C-rich region of the nebula, simultaneous FTT reactions could have generated the graphitic material observed in the track 183 terminal particle. Shock processing of the grain could have produced the necessary high temperatures, while vaporization of adsorbed water-ice could have produced local, surface-oxidizing conditions. The low Ni content and lack of detectable Co also indicate that the metal precursor grain was not typical chondritic metal, but would have initially condensed in a highly reduced region of the nebula, similar to low-Ni-metal in EH3 chondrites. Thus, although the actual construction of the terminal particle is an oxidative process, our observations suggest that the precursors and oxidation mechanism are indicative of formation in a reduced, C-rich region of the solar nebula.

For most planetary materials, geochemical indicators of oxygen fugacity suggest relatively oxidizing conditions (Krot et al. 2000). Enstatite chondrites and aubrite achondrites are exceptions, whose reduced mineral assemblages are consistent with parent-body formation in an environment with $0.95 < C/O < 1.00$ (Keil 1968; Krot et al. 2000). Similarly, the crustal composition of Mercury implies differentiation of a highly reduced bulk composition (Nittler et al. 2011; Zolotov et al. 2013). Considering the condensation and oxidation processes that most likely generated the track 183 assemblage, enstatite chondrites could potentially preserve similar nanoscale nebular assemblages. Currently, the combination of PGC-coated cohenite and Cr-rich magnetite has not been observed in enstatite chondrite matrix, and thus the track 183 terminal particle cannot be tied conclusively to the same parent bodies. However, it does provide further cometary evidence that highly reducing conditions existed in localized regions of the solar nebula. Since the PGC + cohenite core-shell grains reported here are not the product of parent-body processes or capture heating, they support the original interpretation of PGC coatings on rare carbide grains observed in chondritic porous IDPs as a product of FTT processes occurring in warm reducing regions of the nebula (Bradley et al. 1984), rather than the current consensus interpretation as a product of heating during atmospheric entry (Keller et al. 2004).

5. Conclusions

A cometary terminal particle from track 183 in the aerogel collector of the *Stardust* mission to comet 81P/Wild 2 is an unusual aggregate of nanoscale Cr-rich magnetite, with opaque inclusions of nanoscale Fe carbide coated with conformal layers of PGC. Although magnetite is an alteration product of primary materials in chondrite meteorites, no evidence of altered primary grains was found. The core-shell carbide + PGC grains are consistent with a FTT formation process, occurring on either primary carbide condensates or metal grains that are converted to carbide during the organic synthesis reactions. Compositionally speaking, the assemblage is consistent with nebular oxidation of reduced, EH3-chondrite-like metal in a water-ice-rich and C-rich environment. Although the nanoparticulate morphology of the magnetite, as well as the absence of relic metal and other oxidation byproducts (e.g., chromite), suggest the possibility that all of the components in the terminal particle could be direct condensates, reaction rates for magnetite condensation are much too sluggish at such low oxygen fugacity to be possible. The presence of this unusual condensation assemblage in comet Wild 2 is further evidence of large-scale radial mixing in the solar nebula, encompassing highly reduced components in warm inner regions of the nebula where accretion of the enstatite chondrite and aubrite achondrite parent bodies, as well as Mercury, may have occurred, and bringing these components outwards to the Kuiper Belt.

The authors wish to acknowledge the *Stardust* curators at NASA Johnson Space Center for their careful preparation of the allocated aerogel wafer from track 183. We also thank the anonymous reviewers for their helpful comments, particularly regarding the possibility of magnetite condensation. This work was funded by the NASA Laboratory Analysis of Returned Samples program. The Advanced Light Source at Lawrence Berkeley National Laboratory is supported by the Director, Office of Science, Office of Basic Energy Sciences, of the U.S. Department of Energy under contract number DE-AC02-05CH11231.

ORCID iDs

Bradley T. De Gregorio  <https://orcid.org/0000-0001-9096-3545>

Larry R. Nittler  <https://orcid.org/0000-0002-5292-6089>

References

- Bell, M. S. 2007, *M&PS*, 42, 935
- Berger, E. L., Zega, T. J., Keller, L. P., & Lauretta, D. S. 2011, *GeCoA*, 75, 3501
- Bockelée-Morvan, D., Gautier, D., Hersant, F., Huré, J.-M., & Robert, F. 2002, *A&A*, 384, 1107
- Bradley, J. P., Brownlee, D. E., & Fraundorf, P. 1984, *Sci*, 223, 56
- Brearley, A. J. 1990, *GeCoA*, 54, 831
- Brett, R. 1966, *Sci*, 153, 60
- Bridges, J. C., Burchell, M. J., Changela, H. C., et al. 2010, *M&PS*, 45, 55
- Brownlee, D., Joswiak, D., & Matrajt, G. 2012, *M&PS*, 47, 453
- Brownlee, D. E. 2014, *AREPS*, 42, 179
- Brownlee, D. E., Tsou, P., Aléon, J., et al. 2006, *Sci*, 314, 1711
- Burchell, M. J., Mann, J., Creighton, J. A., et al. 2006, *M&PS*, 41, 217
- Busemann, H., Alexander, C. M. O'D., & Nittler, L. R. 2007, *M&PS*, 42, 1387
- Changela, H. G., Bridges, J. C., & Gurman, S. J. 2012, *GeCoA*, 98, 282
- Charon, E., Aléon, J., & Rouzaud, J.-N. 2014a, *GeCoA*, 142, 224
- Charon, E., Rouzaud, J.-N., & Aléon, J. 2014b, *Carbon*, 66, 178
- Ciesla, F. J. 2007, *Sci*, 318, 613
- Ciesla, F. J., & Sandford, S. A. 2012, *Sci*, 336, 452

- Cody, G. D., Ade, H., Alexander, C. M. O'D., et al. 2008a, *M&PS*, **43**, 353
- Cody, G. D., Alexander, C. M. O'D., Yabuta, H., et al. 2008b, *E&PSL*, **272**, 446
- Connolly, H. C., Jr., Huss, G. R., & Wasserburg, G. J. 2001, *GeCoA*, **65**, 4567
- De Gregorio, B. T., Stroud, R. M., Cody, G. D., et al. 2011, *M&PS*, **46**, 1376
- De Gregorio, B. T., Stroud, R. M., Nittler, L. R., et al. 2013, *M&PS*, **48**, 904
- Ebel, D. S. 2006, in *Meteorites and the Early Solar System II*, ed. D. S. Lauretta & H. Y. McSween, Jr. (Tucson, AZ: Univ. Arizona Press), 253
- Ebel, D. S., & Alexander, C. M. O'D. 2011, *P&SS*, **59**, 1888
- Ebel, D. S., & Grossman, L. 2000, *GeCoA*, **64**, 339
- El Goresy, A., Yabuki, H., Ehlers, K., Woolum, D., & Pernicka, E. 1988, in *Proc. NIPR Symp. 1, Twelfth Symp. on Antarctic Meteorites*, ed. I. Kushiro et al. (Tokyo: NIPR), 65
- El Goresy, A., Zinner, E., & Marti, K. 1995, *Natur*, **373**, 496
- Floss, C., Stadermann, F. J., Kearsley, A. T., Burchell, M. J., & Ong, W. J. 2013, *ApJ*, **763**, 140
- Frank, D. R., Zolensky, M. E., & Le, L. 2014, *GeCoA*, **142**, 240
- Fries, M., Burchell, M., Kearsley, A., & Steele, A. 2009, *M&PS*, **44**, 1465
- Greenwood, R. C., Franchi, I. A., Kearsley, A. T., & Alard, O. 2010, *GeCoA*, **74**, 1684
- Harries, D. 2016, in *Proc. 79th Annual Meeting of the Meteoritical Society (Berlin: Lunar and Planetary Institute)*, 6191, <https://www.hou.usra.edu/meetings/metsoc2016/pdf/6191.pdf>
- Hauver, K. L., & Ruzicka, A. M. 2011, in *LPSC XLII (The Woodlands, TX: Lunar and Planetary Institute)*, 2627, <http://www.lpi.usra.edu/meetings/lpsc2011/pdf/2627.pdf>
- Hayatsu, R., & Anders, E. 1981, in *Cosmo- and Geochemistry*, ed. F. L. Boschke (Berlin: Springer), 1
- Herbstein, F. H., & Smuts, J. 1964, *AcCr*, **17**, 1331
- Hicks, L. J., MacArthur, J. L., Bridges, J. C., et al. 2017, *M&PS*, **52**, 2075, doi:10.1111/maps.12909
- Hong, Y., & Fegley, B. 1998, *M&PS*, **33**, 1101
- Horstmann, M., Humayun, M., Fischer-Gödde, M., Bischoff, A., & Weyrauch, M. 2014, *M&PS*, **49**, 1948
- Hua, X., & Buseck, P. R. 1998, *M&PS*, **33**, A215
- Humayun, M., Goldstein, J. I., Mubarak, A., et al. 2015, in *LPSC XLVI (The Woodlands, TX: Lunar and Planetary Institute)*, 2298, <http://www.hou.usra.edu/meetings/lpsc2015/pdf/2298.pdf>
- Isambert, A., De Resseguier, T., Gloter, A., et al. 2006, *E&PSL*, **243**, 820
- Jacob, D., Stodolna, J., Leroux, H., Langenhorst, F., & Houdellier, F. 2009, *M&PS*, **44**, 1475
- Jacobsen, C., Wirrick, S., Flynn, G. J., & Zimba, C. 2000, *JMic*, **197**, 173
- Jones, R. H., & Danielson, L. R. 1997, *M&PS*, **32**, 753
- Joswiak, D. J., Brownlee, D. E., & Matrajt, G. 2012, *M&PS*, **47**, 471
- Joswiak, D. J., Nakashima, D., Brownlee, D. E., et al. 2014, *GeCoA*, **144**, 277
- Keil, K. 1968, *JGR*, **73**, 6945
- Keller, L. P. 1998, *M&PS*, **33**, 913
- Keller, L. P., Messenger, S., Flynn, G. J., et al. 2004, *GeCoA*, **68**, 2577
- Kilcoyne, A. L., Tylliszczak, T., Steele, W. F., et al. 2003, *Journal of Synchrotron Radiation*, **10**, 125
- Krot, A. N., Fegley, B., Jr., Lodders, K., & Palme, H. 2000, in *Protostars and Planets IV*, ed. V. Mannings, A. P. Boss, & S. S. Russell (Tucson, AZ: Univ. Arizona Press), 1019
- Krot, A. N., Zolensky, M. E., Wasson, J. T., et al. 1997, *GeCoA*, **61**, 219
- Kurat, G., Zinner, E., & Brandstätter, F. 2002, *GeCoA*, **66**, 2959
- Lauretta, D. S., & Schmidt, B. E. 2009, *Oxidation of Metals*, **71**, 219
- Le Guillou, C., Rouzaud, J.-N., Bonal, L., et al. 2012, *M&PS*, **47**, 345
- Leitner, J., Hoppe, P., & Heck, P. R. 2010, in *LPSC XLI (The Woodlands, TX: Lunar and Planetary Institute)*, 1607, <http://www.lpi.usra.edu/meetings/lpsc2010/pdf/1607.pdf>
- Leroux, H., Libourel, G., Lemelle, L., & Guyot, F. 2003, *M&PS*, **38**, 81
- Leroux, H., Rietmeijer, F. J. M., Velbel, M. A., et al. 2008, *M&PS*, **43**, 97
- Love, S. G., & Brownlee, D. E. 1991, *Icar*, **89**, 26
- Matrajt, G., Ito, M., Wirrick, S., et al. 2008, *M&PS*, **43**, 315
- Matrajt, G., Messenger, S., Joswiak, D., & Brownlee, D. 2013, *GeCoA*, **117**, 65
- Matzel, J. E. P., Ishii, H. A., Joswiak, D., et al. 2010, *Sci*, **328**, 483
- McCoy, T. J., Carlson, W. D., Nittler, L. R., et al. 2006, *GeCoA*, **70**, 516
- McKeegan, K. D., Aléon, J., Bradley, J., et al. 2006, *Sci*, **314**, 1724
- Mikouchi, T., Tachikawa, O., Hagiya, K., et al. 2007, in *LPSC XXXVIII (Houston, TX: Lunar and Planetary Institute)*, 1946, <http://www.lpi.usra.edu/meetings/lpsc2007/pdf/1946.pdf>
- Mostafaoui, S., Perron, C., Zinner, E., & Sagon, G. 2000, *GeCoA*, **64**, 1945
- Nakamura, T., Noguchi, T., Tsuchiyama, A., et al. 2008, *Sci*, **321**, 1664
- Nakamura-Messenger, K., Keller, L. P., Clemett, S. J., Messenger, S., & Ito, M. 2011, *M&PS*, **46**, 1033
- Nakashima, D., Ushikubo, T., Joswiak, D. J., et al. 2012, *E&PSL*, **357**, 355
- Nakashima, D., Ushikubo, T., Kita, N. T., et al. 2015, *E&PSL*, **410**, 54
- Niemantsverdriet, J. W., Van der Kraan, A. M., Van Dijk, W. L., & Van der Baan, H. S. 1980, *JPhCh*, **84**, 3363
- Nittler, L. R., Starr, R. D., Weider, S. Z., et al. 2011, *Sci*, **333**, 1847
- Nuth, J. A., III, Johnson, N. M., & Manning, S. 2008, *ApJL*, **673**, L225
- Nuth, J. A., III, Kimura, Y., Lucas, C., Ferguson, F., & Johnson, N. M. 2010, *ApJL*, **710**, L98
- Ogliore, R. C., Butterworth, A. L., Fakra, S. C., et al. 2010, *E&PSL*, **296**, 278
- Ogliore, R. C., Huss, G. R., Nagashima, K., et al. 2012, *ApJL*, **745**, L19
- Quirico, E., Raynal, P., & Bourot-Denise, M. 2003, *M&PS*, **38**, 795
- Rambaldi, E. R., & Wasson, J. T. 1982, *GeCoA*, **46**, 929
- Ramdohr, P. 1973, *The Opaque Minerals in Stony Meteorites* (Amsterdam: Elsevier)
- Raupp, G. B., & Delgass, W. N. 1979, *Journal of Catalysis*, **58**, 348
- Remusat, L., Rouzaud, J.-N., Charon, E., et al. 2012, *GeCoA*, **96**, 319
- Rietmeijer, F. J. M. 1992, *GeCoA*, **56**, 1665
- Rietmeijer, F. J. M., & Mackinnon, I. D. R. 1985, *Natur*, **315**, 733
- Rietmeijer, F. J. M., Nakamura, T., Tsuchiyama, A., et al. 2008, *M&PS*, **43**, 121
- Righter, K., & Neff, K. E. 2007, *PolSc*, **1**, 25
- Rubin, A. E. 1997, *MinM*, **61**, 699
- Sakamoto, N., Seto, Y., Itoh, S., et al. 2007, *Sci*, **317**, 231
- Sandford, S. A., Aléon, J., Alexander, C. M. O'D., et al. 2006, *Sci*, **314**, 1720
- Scott, E. R., & Jones, R. H. 1990, *GeCoA*, **54**, 2485
- Scott, E. R. D., Rubin, A. E., Taylor, G. J., & Keil, K. 1981a, *E&PSL*, **56**, 19
- Scott, E. R. D., Taylor, G. J., Rubin, A. E., Okada, A., & Keil, K. 1981b, *Natur*, **291**, 544
- Seto, Y., Sakamoto, N., Fujino, K., et al. 2008, *GeCoA*, **72**, 2723
- Shibata, Y. 1996, *Proc. NIPR Symp. 9, Twentieth Symp. on Antarctic Meteorites*, ed. H. Kojima et al. (Tokyo: NIPR), 79
- Stadermann, F. J., Hoppe, P., Floss, C., et al. 2008, *M&PS*, **43**, 299
- Stodolna, J., Gainsforth, Z., Butterworth, A. L., & Westphal, A. J. 2014, *E&PSL*, **388**, 367
- Stodolna, J., Jacob, D., & Leroux, H. 2012, *GeCoA*, **87**, 35
- Stroud, R. M., Koch, I. M., Bassim, N. D., Piccard, Y. N., & Nittler, L. R. 2010, in *LPSC XLI (The Woodlands, TX: Lunar and Planetary Institute)*, 1792, <http://www.lpi.usra.edu/meetings/lpsc2010/pdf/1792.pdf>
- Thomas-Keptra, K. L., Bazylnski, D. A., Kirschvink, J. L., et al. 2000, *GeCoA*, **64**, 4049
- Weisberg, M. K., & Kimura, M. 2012, *ChEG*, **72**, 101
- Wirrick, S., Flynn, G. J., Keller, L. P., et al. 2009, *M&PS*, **44**, 1611
- Wyckoff, R. W. G. 1963, *Crystal Structures*, Vol. 1 (2nd ed.; New York, NY: Wiley)
- Zolensky, M., Nakamura-Messenger, K., Rietmeijer, F., et al. 2008, *M&PS*, **43**, 261
- Zolotov, M. Y., Sprague, A. L., Hauck, S. A., et al. 2013, *JGRE*, **118**, 138